



HAL
open science

Scaling laws and similarity models for the preliminary design of multirotor drones

Marc Budinger, Aurélien Reysset, Aitor Ochotorena, Scott Delbecq

► **To cite this version:**

Marc Budinger, Aurélien Reysset, Aitor Ochotorena, Scott Delbecq. Scaling laws and similarity models for the preliminary design of multirotor drones. *Aerospace Science and Technology*, 2020, 98, pp.1-15. 10.1016/j.ast.2019.105658 . hal-02997598

HAL Id: hal-02997598

<https://hal.science/hal-02997598>

Submitted on 10 Nov 2020

HAL is a multi-disciplinary open access archive for the deposit and dissemination of scientific research documents, whether they are published or not. The documents may come from teaching and research institutions in France or abroad, or from public or private research centers.

L'archive ouverte pluridisciplinaire **HAL**, est destinée au dépôt et à la diffusion de documents scientifiques de niveau recherche, publiés ou non, émanant des établissements d'enseignement et de recherche français ou étrangers, des laboratoires publics ou privés.



Open Archive Toulouse Archive Ouverte (OATAO)

OATAO is an open access repository that collects the work of some Toulouse researchers and makes it freely available over the web where possible.

This is an author's version published in: <https://oatao.univ-toulouse.fr/26688>

Official URL : <https://doi.org/10.1016/j.ast.2019.105658>

To cite this version :

Budinger, Marc and Reysset, Aurélien and Ochotorena, Aitor and Delbecq, Scott Scaling laws and similarity models for the preliminary design of multicopter drones. (2020) *Aerospace Science and Technology*, 98. 1-15. ISSN 1270-9638

Any correspondence concerning this service should be sent to the repository administrator:

tech-oatao@listes-diff.inp-toulouse.fr

Scaling laws and similarity models for the preliminary design of multirotor drones

M. Budinger^{a,*}, A. Reysset^a, A. Ochotorena^a, S. Delbecq^b

^a ICA, Université de Toulouse, UPS, INSA, ISAE-SUPAERO, MINES-ALBI, CNRS, 3 rue Caroline Aigle, 31400 Toulouse, France

^b ISAE-SUPAERO, Université de Toulouse, 10 Avenue Edouard Belin, 31400 Toulouse, France

A B S T R A C T

Multirotor drones modelling and parameter estimation have gained great interest because of their vast application for civil, industrial, military and agricultural purposes. At the preliminary design level the challenge is to develop lightweight models which remain representative of the physical laws and the system interdependencies. Based on the dimensional analysis, this paper presents a variety of modelling approaches for the estimation of the functional parameters and characteristics of the key components of the system. Through this work a solid framework is presented for helping bridge the gaps between optimizing idealized models and selecting existing components from a database. Special interest is given to the models in terms of reliability and error. The results are compared for various existing drone platforms with different requirements and their differences discussed.

Keywords:

Multirotor drones
Scaling laws
Dimensional analysis
Surrogate models
Propulsion system
Landing gear

1. Context

During the last decade, technological innovations [1–3] have significantly contributed to the development of smart and powerful multirotor UAVs: miniaturization and microelectronic with the integration of inertial sensors, increased computational power of control processors, new battery technologies with higher energy density, permanent magnet motors with higher torque density and high power densities electric-converters.

The expansion of drones market has led to the decrease of drone sizes and the increase of the availability of drone components at very competitive prices. This has facilitated the experimentation and optimization of drone designs based on successive physical tests. Most of recent designs address very specific application-cases with particular performances/needs for which a design optimization process is needed. The design optimization process becomes mandatory when the payload scale factor differs from market trend. Particularly in research projects of large multirotor UAVs designed for the transport of commercial loads or passengers [4–7] where expensive prototypes are used, it is suggested to perform advanced design studies before manufacturing, integration and testing. To accelerate the design process, a general trend is to extend the role of modelling in design and specification. The present paper proposes a set of efficient prediction models

which can be integrated into any optimization tool for rapid preliminary design of multirotor drones [8,9].

Section 2 places emphasis on the sizing scenarios that influence the design of the components and introduces the concept of dimensional analysis for the creation of estimation models. Models based on similarities, also called scaling laws, are described in section 3 and applied in section 4 for the electrical components: motor, battery, ESC and cables.

Regression models are described in section 5 and can adopt different forms: polynomial forms exemplified in section 6 for propellers and variable power law models in section 7 for structural components.

Finally, in section 8 several examples of existing drone platforms are compared with the results obtained using the models.

2. Needs for prediction models during preliminary design

Within the whole product development process, the purpose of preliminary design phase is the evaluation of architecture feasibility, technology selection and components high-level specifications definition based on product requirements and operational scenarios. Yet, to do so, the critical scenarios should be identified and the associated main components characteristics identified.

2.1. Multirotor main components

Fig. 1 shows a typical mass distribution for the different components of a drone according to several examples [10–12]. This paper

* Corresponding author.

E-mail address: marc.budinger@insa-toulouse.fr (M. Budinger).

Nomenclature

ABS	Acrylonitrile Butadiene Styrene
DC	Direct Current
DoE	Design of Experiments
EMF	ElectroMotive Force
ESC	Electronic Speed Controller
FEM	Finite Element Method
IGBT	Insulated Gate Bipolar Transistor
LiPo	Lithium-Polymer
LG	Landing Gear
MTOW	Maximum Takeoff Weight
MOSFET	Metal Oxide Semiconductor Field Effect Transistor
PBS	Product Breakdown Structure
RSM	Response Surface Model
UAV	Unmanned Aerial Vehicle
VPLM	Variable Power Law Metamodel

Latin formula symbols

B	Flux density	T
B_r	Magnetic remanence	T
C	Capacity	Ah
C_{rate}	C-rate	h^{-1}
C_p	Power coefficient	
C_T	Thrust coefficient	
D	Blade diameter	m
E	No-load voltage	V
h	Convection coefficient	$\frac{W}{m^2 K}$
H_{arm}	Arm height	m
I_O	No-load current	A
J	Advance ratio	
J	Winding current density	$\frac{A}{m^2}$
K	Air compressibility	$\frac{N}{m^2}$

k_{eq}	Equivalent stiffness	$\frac{N}{m^2}$
K_T	Torque constant	$\frac{Nm}{A}$
K_V	Velocity constant	$\frac{rpm}{V}$
L	Characteristic length	m
l_{arm}	Arm length	m
M	Mach number	
M	Mass	kg
n_p	Parallel branches	
n_s	Series branches	
n_T	Coil turns	
P_{iron}	Iron losses	W
P_{on}	Conduction losses	W
P_{switch}	Commutation losses	W
r	Diameter ratio	m
R	Resistance	Ω
U	Voltage	V
U_{DC}	DC voltage	V
T_f	Friction torque	Nm
T_{nom}	Nominal torque	Nm
V	Flight speed	$\frac{m}{s}$
V_{impact}	Impact speed	$\frac{m}{s}$

Greek formula symbols

β	Ratio pitch-to-diameter	
δ	Rotational speed	$\frac{rad}{s}$
ϵ	Average relative error	%
ω	Rotational speed	$\frac{rad}{s}$
π	Dimensionless number	
ρ	Resistivity	Ωm
σ	Standard deviation	%
θ	Maximum admissible temperature	K

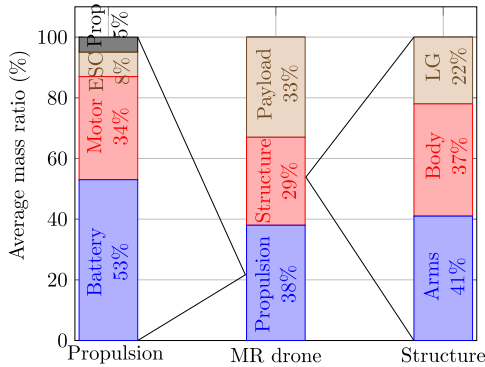


Fig. 1. Multirotor drone average mass distribution based on [10–12].

deals with propulsion, energy, power conversion and storage components generally treated in a non-homogeneous way in different papers but also addresses structural parts. All these parts have a significant impact on global mass which is strongly coupled with autonomy and dynamic performances. The control aspects and associated sensors are not considered here.

2.2. Design drivers and sizing scenarios

The main performance requirements for drones are (regardless of the control-laws): the payload mass, forward speed, hover autonomy or range [13]. In addition to these system level power-energy considerations, the components must withstand some transitory extreme or endurance criteria that request specific knowl-

edge of the technology or physical-domain. The so-called components design drivers are summarized in Table 1 with the corresponding scenarios for which they should be assessed as well as literature references.

2.3. Dimensional analysis and Buckingham's theorem

Some references [19] or tools [20] directly use databases to evaluate the performance resulting from the association of defined components. The explosion of combinatorial solutions which increase with the databases size may lead to very high computation time. This is why, most of the design methodologies, despite the wide variety of implementations [9,16,8], are based on analytical expressions or catalogue data regressions and benefit, as most continuous problems, of numerical optimization capabilities and high convergence performance.

Dimensional analysis and Buckingham's theorem [21,22] are extensively used in aerodynamics and fluid mechanics to provide a more physical and unified framework for all the components and their corresponding characteristics. This paper shows how it can be extended to other domains by addressing all the components of a drone.

The fundamental step is to express one component characteristic y as an algebraic function f of geometrical dimensions and physical/material properties:

$$y = f(\underbrace{L, d_1, d_2, \dots}_{\text{geometric}}, \underbrace{p_1, p_2, \dots}_{\text{physical}}) \quad (1)$$

Table 1
Design drivers and sizing scenarios.

Components	Design drivers	Parameters or characteristics	Sizing scenario segment	Ref.
Propeller	Max thrust	Diameter, tip speed	Takeoff and high power mission segment	[14]
	Efficiency	Pitch	Hover and long duration mission segment	[14]
Motor	Temperature rise	Nominal torque, Resistance	Hover and long duration mission segment	[15]
	Max voltage	Torque constant, Resistance	Takeoff and high power mission segment	[16]
ESC	Temperature rise	Max power, max current	Takeoff and high power mission segment	[16]
Battery	Energy	Voltage, capacity	Hover flight (autonomy) and forward mission segment (range)	[14]
	Power	Max discharge rate	Takeoff and high power mission segment	[16]
Frame	Stress	Mechanical strength	Takeoff and landing	[17]
	Vibration	Resonance frequency	Takeoff and high power mission segment	[18]

with L as the characteristic length and d_i and p_i as the rest of geometric and physical parameters.

The Buckingham's theorem states that the original equation (1), with n parameters and u physical units (time, mass, length...), can be rewritten with a reduced set of $n - u$ dimensionless parameters called π numbers:

$$\pi_y = f'(\pi_{d1}, \pi_{d2}, \dots, \pi_{p1}, \pi_{p2}, \dots) \quad (2)$$

where:

$$\pi_y = y^{a_y} \cdot L^{a_L} \prod_i p_i^{a_i} \quad (3)$$

$$\pi_{di} = \frac{d_i}{L} \quad (4)$$

$$\pi_{pi} = L^{a_{pi,0}} \prod_j p_i^{a_{pi,j}} \quad (5)$$

Therefore, the dimensional analysis and the Buckingham theorem can permit to reduce the number of input parameters of a numerical model and hence its complexity and computational cost.

The estimation model used will depend on the character of the dimensionless number. Scaling laws are commonly used when π_{di} and π_{pi} stay constant in the range of a series, for example for the sizing of the electrical components. When the components do not comply with a geometrical or material similarity, then alternative forms will be applied such as regression models for the study of the propeller parameters or the structural parts.

An overview of the process is shown in Fig. 2.

3. Scaling laws

The scaling laws, also called similarity laws or allometric models, are based on the dimensional analysis. These simplification laws are really interesting in a preliminary design process because they limit drastically the number of design parameters for each component while having good estimation properties based on a

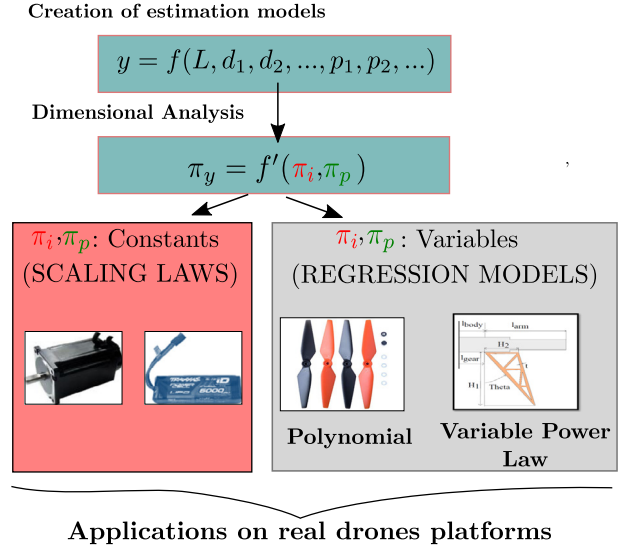


Fig. 2. Estimation models of drone components based on dimensional analysis.

detailed reference component. These laws are established assuming:

- **Geometric similarity:** all the length ratios between the current component and its corresponding reference are constant. With this assumption the aspect ratios $\pi_{di} = \frac{d_i}{L}$ are constant,
- **Uniqueness of design driver:** only one main dominant physical phenomenon drives the evolution of the secondary characteristic y . With this assumption, the number of π_{pi} is equal to zero,
- **Material similarity:** all material and physical properties are assumed to be identical to those of the component as the reference. If the number of π_{pi} is not equal to zero, the remaining dimensionless numbers can often be expressed through constant ratios of material properties with similar units.

If these assumptions are satisfied, the resulting π_{di} and π_{pi} dimensionless numbers are constant and consequently to π_y :

$$\pi_y = yL^{a_L} \prod_{i=1}^m p_i^{a_i} = \text{constant} \quad (6)$$

which gives the typical power law form of scaling laws:

$$y \propto L^a \Leftrightarrow y^* = L^{*a} \Leftrightarrow \frac{y}{y_{ref}} = \left(\frac{L}{L_{ref}} \right)^a \quad (7)$$

where a is a constant representative of the problem. This paper also uses the notation proposed by M. Jufer in [23] where a scaling ratio x^* of a given parameter is calculated as $x^* = \frac{x}{x_{ref}}$. The scaling laws present the asset of requiring only one reference component to extrapolate component characteristics (written $_{ref}$) on a wide range of exploration. More information on the construction, validation and use of scaling laws for engineering purposes can be found in [24]. Scaling laws are used in this paper for the modelling of electrical components: brushless motors, inverters - part of ESCs and the battery.

3.1. Uncertainty of scaling models

This article will provide the set of standard deviations of estimation errors for each proposed model. In order to be able to better use these quantities, especially for uncertainty propagation

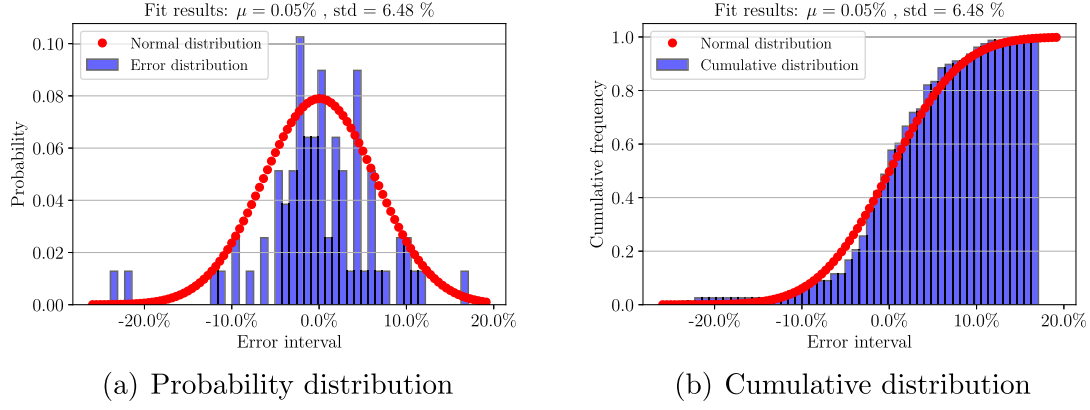


Fig. 3. Comparison of error distribution to a normal law. (For interpretation of the colours in the figure(s), the reader is referred to the web version of this article.)

or robust optimization, we will show here that errors distributions for scaling laws can be modelled as independent normal laws.

Assuming the scaling law is defined as:

$$\tilde{y} = k \cdot x^a$$

where x is the definition variable and \tilde{y} is the estimated parameter of the studied component. The following relationship is used to predict the estimated error between the real variable and the estimated one:

$$y = \tilde{y}(1 + \varepsilon)$$

ε is modelled as a random variable. Possible error sources may be related to multiple factors, such as the assumption of the geometric similarity for much larger dimensions, unfeasibility regarding some design constraints, changing materials or physical properties.

The normal distribution is the most common method used to model phenomena with multiple random events. For this method, the probability density follows a Gaussian distribution:

$$f(\varepsilon) = \frac{1}{\sigma\sqrt{2\pi}} e^{-\frac{1}{2}\left(\frac{\varepsilon-\mu}{\sigma}\right)^2}$$

where μ is the mean and σ the standard deviation. An example of such distribution is illustrated in Fig. 3. The histogram shows the distribution of the relative error for the estimated battery mass for different references of Lithium-Polymer batteries.

A graphical technique used to assess the adequacy of the observed distribution to a Gaussian distribution is the normal probability plot. This method fits a set of observations to a straight line and those deviations found from the straight line are variations from the normal law. The mean and the standard deviation are read on the abscissa from the crossing of the interpolation line with $Y = 0$ and $Y = 1$ respectively. The collected data series fit properly to a normal distribution as depicted in Fig. 4 with a mean value $\mu = 0.05\%$ and standard deviation value $\sigma = 6.48\%$.

In order to minimize the error of estimation when applying scaling laws, it is recommended to take into account some factors. The main factors or good practices are:

- Choice of a mid-range reference point

The choice of a good reference value will have a strong effect on the scaling law as it will keep the mean error as low as possible. Scaling laws follow, as discussed before, a normal distribution where choosing a reference of the extremes entails a difference increase for the other values. The next figure shows the evolution of the relative error according to the different motor torque (Fig. 5). It is observed that the error tends to decrease for references which are close to the geometric mean of minimum and maximum values of the full range.

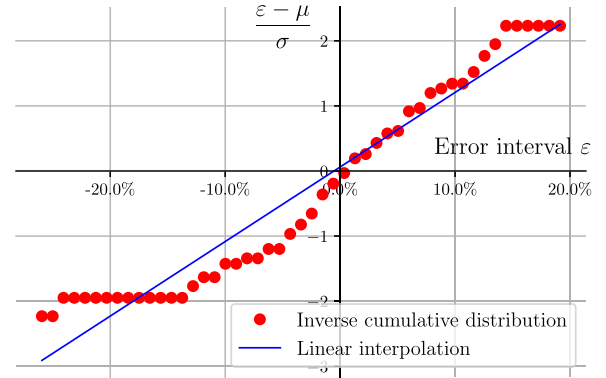


Fig. 4. Normal probability plot.

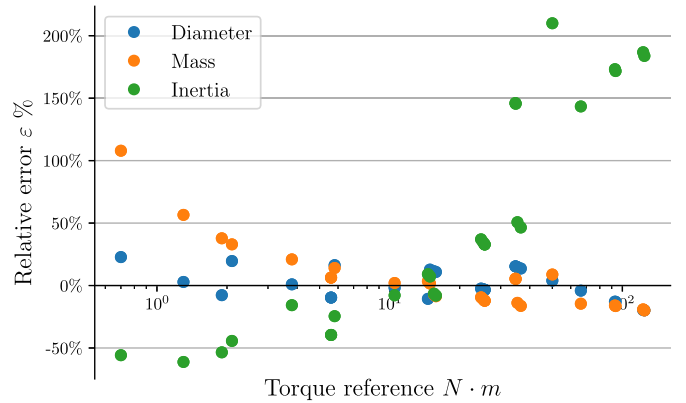


Fig. 5. Effect of the reference point choice on the mean error (motor example).

- Correlation between errors

Uncertainties from the different estimation models may be linked to further random variables or independent to its own random variable. The dependency is studied using a correlation analysis. An example is applied for the following motor equations:

$$M_{mot} = M_{mot.ref} \left(\frac{T_{mot}}{T_{mot.ref}} \right)^{3/3.5} \quad \text{Motor mass}$$

$$T_{mot.fr} = T_{mot.fr.ref} \left(\frac{T_{mot}}{T_{mot.ref}} \right)^{3/3.5} \quad \text{Motor friction torque}$$

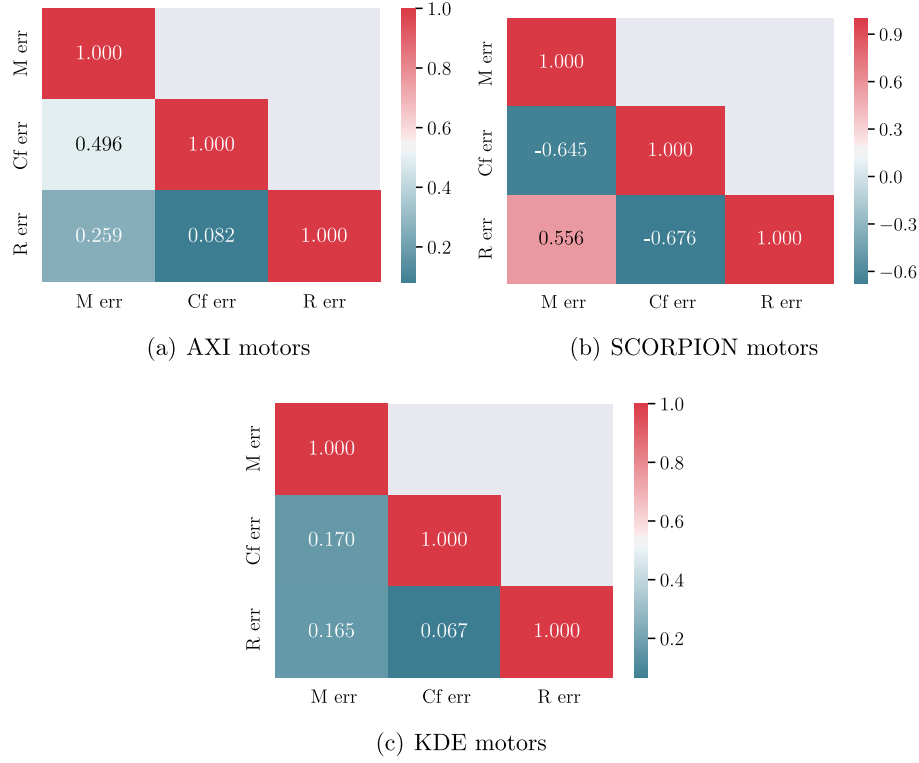


Fig. 6. Correlation of errors between different motor models.

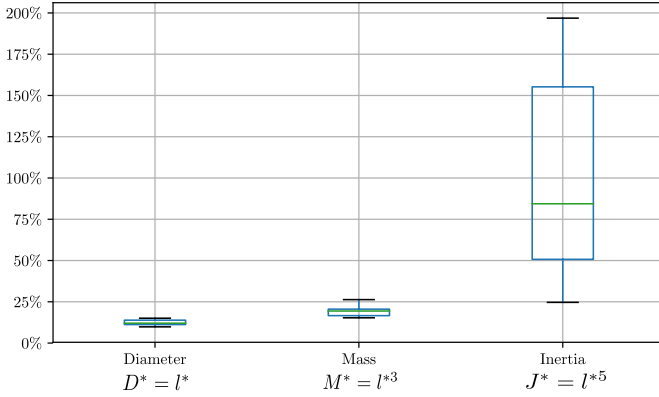


Fig. 7. Standard deviation associated to geometrical parameters.

$$R_{max,mot} = R_{max,mot,ref} \left(\frac{K_T}{K_{T,ref}} \right)^2 \left(\frac{T_{mot}}{T_{mot,ref}} \right)^{-5/3.5} \text{ Motor resistance}$$

After a correlation analysis for different motor models, it is clear that there is no clear relationship found between the different variables. Hence, it is assumed that the errors are independent (Fig. 6).

- **Form of the equation**

For scaling laws linked directly to some geometric parameters, it can be noted that uncertainty of a dimension may grow with increasing power. Fig. 7 outlines the distribution of the standard deviation for all references of the BH range from the manufacturer Kollmorgen.

In the absence of more information, if the scaling laws are related to geometric parameters, the estimation of uncertainties is directly related to the exponent of the scaling law as for the present example: 10% for the diameter, 30% mass and 50% inertia.

4. Scaling laws applied to electrical components

4.1. Brushless motor

Many papers [9,16,8] use direct regressions upon manufacturer datasheets. Here, we outline how scaling laws can represent the same information from a single reference and with similar fidelity while enhancing understanding of major physical and/or technological effects.

4.1.1. Design drivers and main parameters

The multirotor UAVs integrate permanent magnet synchronous motors with an internal (in-runner) or external (out-runner) rotor. As encountered on the current drone market, most solutions use out-runner type which directly drives the propeller. Thus, only a model adapted to such type is presented hereafter.

Manufacturers provide technical information in the form of equivalent DC motor such as:

- The constant velocity K_v which is generally expressed in $\left[\frac{rpm}{V} \right]$. This constant is related to the speed or the torque constant $K_T = \frac{60}{2\pi \cdot K_v}$ (equivalent units $\left[\frac{Nm}{A} \right]$ or $\left[\frac{V}{rad/s} \right]$ from which it is possible to express the torque $T = K_T \cdot I$ with respect to the current I or the no load voltage $E = K_T \cdot \omega$ with respect to the speed ω ,
- The continuous current related to the continuous torque T_{nom} which is limited by motor losses and heat dissipation,
- A maximum transient current (or torque T_{max}) which is linked to the maximum losses and potentially maintained for a few seconds or a few tens of seconds,
- The no-load current I_0 which represents the motor no-load losses. For high speed and high poles number motors, these losses are mainly iron losses that increase with rotational speed,

Table 2
Dimensional analysis on Equation (8).

Parameter	[Voltage]	[Current]	[Length]	[Temperature]
$J \left[\frac{\text{A}}{\text{m}^2} \right]$	0	1	-2	0
$\rho \left[\frac{\Omega}{\text{m}} \right]$	1	-1	1	0
$\theta \text{ [K]}$	0	0	0	1
$h \left[\frac{\text{W}}{\text{m}^2 \text{K}} \right]$	1	1	-2	-1
$L \text{ [m]}$	0	0	1	0
$d_1 \text{ [m]}$	0	0	1	0
$d_2 \text{ [m]}$	0	0	1	0

Table 3
Dimensional analysis on Equation (9).

Parameter	[Force]	[Length]	[Current]
$T \text{ [Nm]}$	1	1	0
$J \left[\frac{\text{A}}{\text{m}^2} \right]$	0	-2	1
$B_r \text{ [Wb]}$	1	-1	1
$L \text{ [m]}$	0	1	0
$d_1 \text{ [m]}$	0	1	0
$d_2 \text{ [m]}$	0	1	0

- The resistance R which causes the ohmic voltage drop and has an effect on the copper losses.

4.1.2. Dimensional analysis and main relations

In this sub-section the construction of scaling laws with dimensional analysis is illustrated on brushless motors. The considered assumptions are that the main design criterion for the motor is the maximum winding temperature and that natural convection is the dominant thermal phenomenon. We use the following notations for the further dimensional analysis:

J : Winding current density d_i : other motor's dimensions L : Motor length ρ : Cooper Resistivity θ : Max. Admissible temperature rise for winding insulation h : Convection coefficient	B_r : Remanent induction permanent magnet Ω : Rotational speed S_f : Magnetic flux motor surface B : Flux density T : Electromagnetic torque
--	---

Considering thermal properties, the current density J can be linked to the motor dimensions and additional material properties:

$$J = f(\underbrace{L, d_1, d_2}_3, \underbrace{\rho, \theta, h}_3) \quad (8)$$

Considering magnetic properties, the torque T can be linked to dimensions and current density,

$$T = f(\underbrace{L, d_1, d_2}_3, \underbrace{J, B_r}_2) \quad (9)$$

Table 2 and Table 3 summarize the dimensional analysis of these equations.

The problem represented by Equation (8) contains 7 parameters and 4 dimensions and can be reduced to 3 dimensionless parameters. We focus on π_J dimensionless parameter which is of the form:

$$\pi_J = J^{a_J} \cdot L^{a_L} \cdot \rho^{a_\rho} \cdot \theta^{a_\theta} \cdot h^{a_h} = J^2 \cdot L^1 \cdot \rho^1 \cdot \theta^{-1} \cdot h^{-1}$$

Equation (8) can then be reduced, using Buckingham's Theorem to:

$$\frac{\rho J^2 L}{h \theta} = f' \left(\frac{d_1}{L}, \frac{d_2}{L} \right) \quad (10)$$

Similar analysis conducts to Equation (9) simplification:

$$\frac{T}{J B_r L^4} = f' \left(\frac{d_1}{L}, \frac{d_2}{L} \right) \quad (11)$$

Considering material and geometric similarities ($\frac{d_i}{L} = \text{constant}$ and $\frac{h \theta}{\rho} = \text{constant}$) the following scaling laws derive from Equations (10) and (11):

$$J \propto L^{-0.5} \Leftrightarrow J^* = L^{*-0.5} \quad (12)$$

$$T \propto J L^4 \Leftrightarrow T^* = J^* \cdot L^{*4} \quad (13)$$

The combination of both previous equations enables the torque to be expressed as a function of the motor size:

$$T \propto L^{3.5} \Leftrightarrow T^* = L^{*3.5} \quad (14)$$

Still considering material/geometrical similarity, the motor mass can be estimated with respect to its torque:

$$M \propto L^3 \propto T^{\frac{3}{3.5}} \Leftrightarrow M^* = T^{*\frac{3}{3.5}} \quad (15)$$

4.1.3. Scaling laws for the electrical parameters

Another approach presented in [23] consists in setting up the scaling laws directly using the analytical expression of the parameter under study. As an example, the electrical circuits including windings should be designed to make their operating voltage compatible with the power source or the power electronics voltage. An analysis [24] of the no-load voltage E gives the back EMF constant K_T as a function of the coil turns number n_t :

$$K_T = \frac{E}{\Omega} = \frac{k \cdot n_t \cdot \Omega \cdot B \cdot S_f}{\omega} \Rightarrow K_T \propto n_t \cdot L^2 \quad (16)$$

K_T does not vary while considering similarity and is a function of motor constants: surface coefficient, filling ratio, winding coefficient, coils number per group, coils number per group and phase, total notches number, notches number per group.

The number of turns n_t is also involved in the resistance R expression:

$$R \propto n_t^2 \cdot L^{-1} \quad (17)$$

this resistance can be used to express copper losses.

Another type of losses can be observed in synchronous motor and are due to induction variation: iron losses. The quantity of iron losses can be expressed according to the Steinmetz-like formula [25] as:

$$P_{iron} \propto f^b \cdot L^3 \quad (18)$$

where f is the electrical frequency linked to the pole number and mechanical rotational speed Ω : leading to friction torque T_f formula:

$$T_f = \frac{P_{iron}}{\Omega} \propto \Omega^{b-1} \cdot L^3 \quad (19)$$

Equation (35) given thereafter shows that the torque is linked to the rotational speed and the propeller diameter. Considering that the propeller is operating at constant tip speed then:

$$\Omega^* = D^{*-1} \Rightarrow T^* = D^{*3} = \Omega^{*-3}$$

This means, if an average value of 1.5 is considered for b , Equation (19) can thus be simplified to:

$$T_f^* = T^{*- \frac{1.5-1}{3}} \cdot T^{*\frac{3}{3.5}} \approx T^{*0.69} \quad (20)$$

Table 4
Scaling laws applied to out-runner brushless motor.

Parameter & equation	AXI ^a		SCORPION ^b		KDE ^c	
	Value	σ [%]	Value	σ [%]	Value	σ [%]
Nominal torque T_{nom}^* [Nm]	0.102		1.84		1.794	
Torque constant K_T^* [$\frac{Nm}{A}$]	0.005		0.029		0.028	
Maximum torque T_{max}^* [Nm] $T_{max}^* = T_{nom}^*$	0.137	N/A	1.88	N/A	1.823	N/A
Friction torque T_f^* [Nm] $T_f^* = \Omega^{b-1} \cdot L^3 \approx T_{nom}^{0.69}$	0.006	15.41	0.041	26.72	0.021	33.4
Mass M^* [g] $M^* = T_{nom}^{*\frac{3}{5}}$	57	11.51	435	10.07	305	9.49
Resistance R^* [Ω] $R^* = K^{*2} \cdot T_{nom}^{*\frac{5}{3}}$	0.045	13.21	0.031	N/A	0.044	N/A

^a AXI Motors: <https://www.modelmotors.cz/e-shop/>.

^b SCORPION: <https://www.scorpionsystem.com/catalog/aeroplane/>.

^c KDE Direct: <https://www.kdedirect.com/collections/uas-multi-rotor-brushless-motors>.

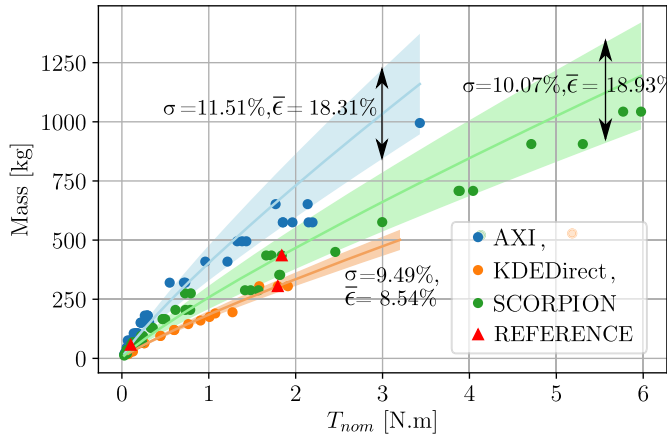


Fig. 8. Mass vs nominal Torque for different motor families.

4.1.4. Scaling laws summary and validation

Table 4 synthesises the previous developed scaling laws for the motors and gives an example of reference data.

In the following Fig. 8, mass data are compared with their corresponding scaling laws. In order to select the best reference point with the lowest possible error with respect to the mass, the average relative error was compared by testing all available data points.

The standard deviation for the mass estimation is between 9.49% and 11.51%. A figure corresponding to the friction torque estimation is not shown here, but the standard deviation is higher (between 15.4% and 33.41%). However, it remains acceptable for a preliminary model.

Since the scaling law for the electrical resistance depends on more than one parameter, the use of a $X = Y$ chart could permit to visualize the estimated values against the database. The standard deviation relative error is 13% for the AXI database.

4.2. Power electronics

For drones, the Electronic Speed Controllers (ESC) distributing power to the synchronous motors are mainly DC/AC converters (inverters) made of power electronic switches (MOSFET transistors). For drone application cases, power MOSFET are preferred to IGBT because of their high commutation frequency and great efficiency even under low voltages.

4.2.1. Design drivers and main parameters

The ESC main components and corresponding main design parameters are listed hereafter. The main criteria influencing the size of the components are related to thermal aspects. The remainder of this section aims at expressing the effect of scaling on the losses and heat transfer properties.

- MOSFET transistors: maximum junction temperature is function of conduction P_{on} , commutation losses P_{switch} and thermal resistance $R_{th_{jc}}$.
- MOSFET driver: Peak gate drive currents influence the commutation losses of MOSFET transistors.
- DC capacitor: stabilizes the voltage but the high-frequency current charge/discharge generates losses.
- Case: Mechanically protects the components but also acts as a heatsink for all internal losses.

4.2.2. Scaling laws approach

MOSFET have two main types of losses [26]:

- Conduction losses: $P_{on} = R_{ds,on} \cdot I_{RMS}^2$ with I_{RMS} the RMS current and $R_{ds,on}$ the ON resistance,
- Switching losses: $P_{switch} \propto U_{DC} \cdot I \cdot \frac{Q_G}{T_G} \cdot f_{switch}$ with $\frac{Q_G}{T_G}$ the commutation time (fraction of gate capacitance and driver gate current).

For low-power transistors and relative low switching-frequency (as this is the case for UAVs application) switching losses can be neglected compared to conduction losses. In addition, we assume that to limit conduction losses, the number of parallel elementary cells used to realize a MOSFET transistor is proportional to the current rating and thus $R_{ds,on} \propto I^{-1}$.

This leads to:

$$P_{loss,MOSFET} \approx P_{ON} \propto I \quad (21)$$

In turn, considering that transistor design is driven by maximum thermal criterion and power dissipation is mainly due to forced convection (caused by propeller air flow, ESC being integrated nearby), we get at equilibrium:

$$\begin{aligned} \Delta\theta &= \frac{1}{h \cdot S} \cdot P_{loss,MOSFET} \implies \Delta\theta^* = 1 = I^{*-2} \cdot I^* \\ &\implies M^* = I^{*3} = I^{*\frac{3}{2}} \end{aligned} \quad (22)$$

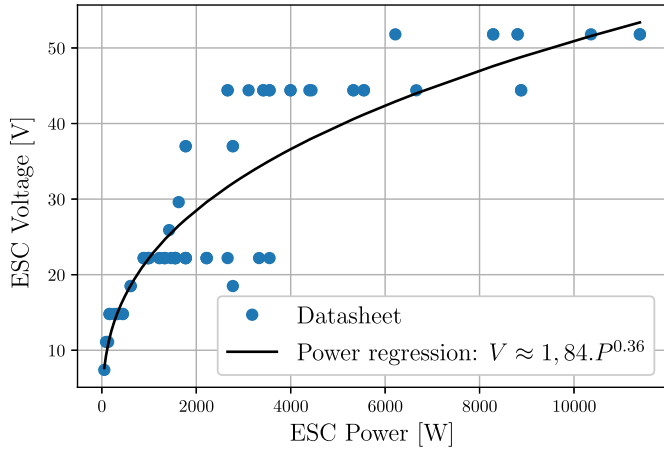


Fig. 9. ESC voltage vs. power regression.

with h the convection coefficient (considered constant), S the convection exchange surface, $\Delta\theta$ the temperature drop constant for a given material or technology and l the converter typical dimension.

The idea is now to link nominal power to the mass instead of current but to do so, the relationship between MOSFET nominal power and voltage has to be determined. Fig. 9 represents the power and voltage of 75 different drone ESCs from Jive, Kosmik, YGE, Spin and Turnigy suppliers. Voltage level increases with power and a direct power-law linking voltage to power is considered here:

$$V^* = P^{*a} \implies V = \frac{V_{ref}}{P_{ref}^a} \cdot P^a = K \cdot P^a \quad (23)$$

$$\implies \log(V) = a \cdot \log(P) + \log(K)$$

The constant K represents a reference component and a the power to be determined. A linear regression is performed into log space and leads to the approximation $V^* = P^{*\frac{1}{3}}$.

Equation (22) can then be modified to:

$$M^* = I^{*\frac{3}{2}} = \left(\frac{P}{V}\right)^{\frac{3}{2}} = P^* \quad (24)$$

This is the main result for modelling the ESC. Yet during design, another representative value extracted from mission profile/sizing scenario (linked to motor/battery performances) is the maximum apparent power:

$$P_{max} = U_{max} \cdot I_{max} = U_{bat} \cdot \max\left(\frac{P_{mot}}{U_{mot}}\right) \quad (25)$$

4.2.3. Scaling laws synthesis and validation

The following Table 5 lists the main scaling laws deduced for the ESC and compares the validity of these models with several families of components. More details on the use of scaling laws for sizing and optimization of static converters can be found in [27, 28].

4.3. Battery pack

An essential step of the preliminary design process for multi-rotor drones is to select a technology and size the battery pack considering missions performances needs. Lemon et al. [29] highlight huge differences between the electrochemical couples but also with the cell design itself (Li-Ion specific energy can be multiplied by 4).

A high discharge rate (or high power density) means high-dynamics capabilities while high energy density stands for high autonomy (long stationary flight). One technology stands out for its high performance capabilities: Lithium-Ion. From this family, the Lithium-Ion Polymer with slightly similar performances but higher life cycle duration and safety (better resistance to over-charge) is taken as a reference.

4.3.1. Design drivers and main parameters

In this sub-section scaling laws based on the analytical expression of the main sizing parameters of a battery are constructed. The laws are valid despite the cell technology chosen:

- **Voltage (U in V):** The batteries are usually a set of cells wired in series to produce the needed voltage (cell voltage being around 3.7 V). When combining n_s batteries in series, total voltage U is the sum of all cells unitary voltage U_{cell} ($U = n_s \cdot U_{cell}$).
- **Capacity (C in Ah):** By connecting batteries in series, capacity does not increase (but stored E energy does: $E = C \cdot U$). When the current capacity needs to be increased n_p branch should be connected in parallel: $C = n_p \cdot C_i$. The battery mass being almost linearly connected to its cells number (packaging put aside), this leads to the main scaling law for a given cell technology:

$$M = n_s \cdot n_p \cdot M_{cell} \implies M^* = U^* \cdot C^* = E^* \quad (26)$$

Table 5
Scaling laws applied to different families of electronic speed controllers (ESC).

Parameters & equation	JIVE ^a		KOSM ^b		YGE ^c		SPIN ^d		TURN ^e	
	Value	σ [%]	Value	σ [%]	Value	σ [%]	Value	σ [%]	Value	σ [%]
ESC voltage V_{ESC}^* [V]	44.4		51.8		51.8		44.4		22.2	
Maximum power P_{max}^* [W]	2664		10360		6216		3419		3330	
Maximum current I_{max}^* [A]	60		200		120		77		150	
Mass M [kg]	84		200		119		105		169	
$M^* = P^*$		13.75		14.14		22.58		19.42		25.36
$M^* = I^{*3/2}$		46.07		20.11		43.98		30.52		21.17

^a JIVE ESC - <http://shyau.com.tw/documents/>.

^b KOSMIK - <https://www.kontronik.com/en/products/speedcontroller/speedcontroller1/kosmik.html>.

^c YGE - <https://www.yge.de/en/home-2/>.

^d SPIN OPTO - <https://www.modelmotors.cz/product/jeti-spin/>.

^e TURNIGY - <http://www.turnigy.com/>.

Table 6
Scaling laws applied to batteries.

Parameters & equation	GENS ^a		PROL ^b		RAMP ^c		TAT ^d		KOK ^e	
	Value	σ [%]	Value	σ [%]	Value	σ [%]	Value	σ [%]	Value	σ [%]
Voltage U^* [V]	22.2		22.2		22.2		11.1		3.7	
Capacity C^* [mAh]	5000		4400		1800		1550		200000	
Mass M [kg] $M^* = C^* \cdot U^*$	755	3.05	601	4.61	291	7.07	128	19.71	4180	3.91

^a GENS ACE (Lithium-Polymer) <https://www.gensace.de/>.

^b PROLITEX (Lithium-Polymer) <http://www.thunderpowerrc.com/>.

^c RAMPAGE (Lithium-Polymer) <http://www.thunderpowerrc.com/Home/Rampage-Series>.

^d TATTU (Lithium-Polymer) <https://www.genstattu.com/>.

^e KOKAM (Lithium-Ion) <http://kokam.com/>.

- **C-rate (C_{rate} in h^{-1}):** Discharge current is often expressed as a C-rate to normalize against battery capacity. A C-rate is a measure of how fast a battery can be discharged relative to its maximum capacity without presenting permanent damage. If $C_{rate} = 1$, then the discharge current will discharge the entire battery in one hour. Formula linking maximum current I_{max} to C-rate is the following:

$$I_{max} = C_{rate} \cdot C \quad (27)$$

For a given cell technology, C_{rate} stays constant and $I_{max}^* = C^*$.

Specific power and energy are assumed to remain constant over a cell assembly even if the packaging can vary on a given series range with no particular correlation to capacity.

4.3.2. Scaling laws synthesis and validation

Table 6 summarizes the previous scaling laws proposed for the batteries and gives examples of reference data. 187 batteries coming from Li-Po and Li-ion are used.

4.4. Electric cables

Electric conductors cross-section area is selected with nominal current. The design driver of such a component is in fact the maximal insulator temperature. The temperature drop is linked to power losses that are mainly due to the Joule effect:

$$P_{loss} \approx P_{loss, Joule} = \rho \cdot J^2 \cdot V \quad (28)$$

where ρ is the resistivity of the conductor, J the current density and V the conductor volume.

It is assumed here that because of the thin insulator thickness, the thermal conduction resistance can be neglected compared to the convection one. This means that the power loss can be linked to insulator exchange area $S = 2\pi \cdot r \cdot L$ (r cable radius and L length):

$$P_{loss} = h \cdot S \cdot \Delta\theta \quad (29)$$

with h the convective heat transfer coefficient and $\Delta\theta$ the admissible temperature drop (constant for a given external temperature and insulator material: $h^* = 1$ and $\Delta\theta^* = 1$).

Equations (28) and (29) lead to the following formulation of the nominal current density (J):

$$J^* = r^{*-1/2} \quad (30)$$

Considering the current is $I = J \cdot S$, current can be expressed as a function of the radius:

Table 7
Scaling laws applied to electric conductors.

Parameters & Equation	Wiring cable ^a	
	Value	σ [%]
Current I [A]	120	
Radius r [mm] $r^* = I^{*2/3}$	5.2	5.56
Linear mass $\frac{M}{L}$ [$\frac{kg}{m}$] $\frac{M}{L} = I^{*4/3}$	0.191	11.08

^a PVC-insulated single wiring cables https://www.engineeringtoolbox.com/wire-gauges-d_419.html.

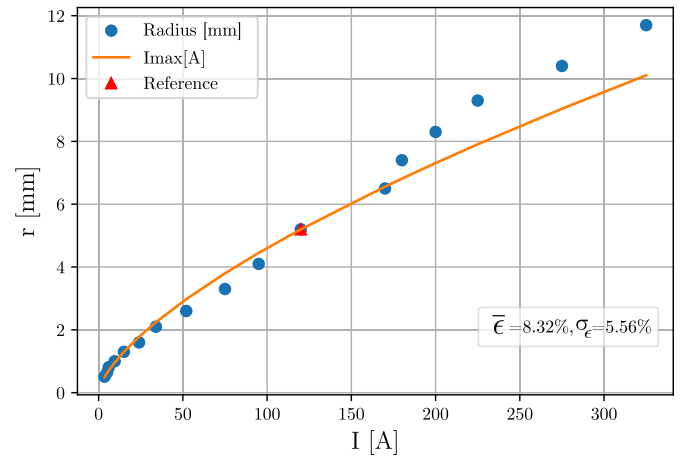


Fig. 10. Radius vs. Current load.

$$I = J \cdot \pi \cdot r^2 \implies r^* = I^{*2/3} \quad (31)$$

Equation (31) can be used to find the relationship between the linear resistance $\frac{R}{L}$ of a wire and its nominal current caliber:

$$\frac{R}{L} = \frac{\rho}{S} \propto r^{-2} \implies \left(\frac{R}{L}\right)^* = I^{*-4/3} \quad (32)$$

At the same time, the linear mass $\frac{M}{L}$ of the conductor can be expressed as a function of r :

$$\left(\frac{M}{L}\right) \propto r^2 \implies \left(\frac{M}{L}\right)^* = I^{*4/3} \quad (33)$$

4.4.1. Scaling laws summary and validation

Table 7 summarizes the scaling laws:

The comparison of these laws with catalogue data yields a mean relative error of 16% for the linear mass and about 8% for the radius (Fig. 10).

Table 8
APC 10 × 4.5 inch multirotor datasheet [32].

n (rpm)	V (mph)	C_T (-)	C_P (-)
2000	0.0	0.1102	0.0428
2000	5.1	0.0832	0.0436
2000	13.1	0.0057	0.0114
6000	0.0	0.1126	0.0432
6000	16.1	0.0822	0.0427
6000	33.5	0.0226	0.0196
10000	0.0	0.1154	0.0485
10000	29.2	0.0789	0.0404
10000	60.7	0.0112	0.0120

5. Regression with dimensionless numbers

In the case where it is not possible to consider as constant the dimensionless numbers π_{di} and π_{pi} , the approximation of the function f can be achieved by performing data regressions [30,31]. The data can come from manufacturer product data as presented in section 5 for the propellers, test measurements or finite element simulations results computed on DoE as presented in section 6 for the drone structure parts. The utilization of π numbers to set up a response surface model (RSM) or a surrogate model has several advantages:

- A decrease in the number of variables to be manipulated and therefore a drastic decrease in physical or numerical experiments to be carried out,
- An increase of the regression robustness [30] in particular if the RSM is built within the logarithmic space as for the VPLM methodology (Variable Power Law Metamodel) [31] which shows good results in interpolation but also in extrapolation because of the power law form.

6. Polynomial regression applied to propeller datasheets

The propeller represents a key component in the drone propulsion chain. Its performance can be expressed as a function of two coefficients C_T and C_P respectively expressing thrust (Equation (34)) and mechanical power (Equation (35)) equations:

$$Thrust = C_T \cdot \rho_{air} \cdot n^2 \cdot D^4 \quad (34)$$

$$Power = C_P \cdot \rho_{air} \cdot n^3 \cdot D^5 \quad (35)$$

where ρ_{air} represents the air density, n the rotational speed [$\frac{rev}{s}$] and D the propeller diameter.

When an engineer is facing a new drone design problem, he can recursively try different propeller references and test performances against different mission profiles (takeoff, dynamic performances/vertical acceleration, range...). In that case, he can interpolate manufacturer datasheets such as the one presented in Table 8 to have an estimate of the performance coefficients for each working condition:

$$C_T = f_t(n, V) \quad (36)$$

$$C_P = f_p(n, V) \quad (37)$$

where V represents the relative air speed.

Nevertheless, as explained before, the performance of the resolution is enhanced while defining continuous expression to estimate the performance coefficients over the whole multirotor dataset.

$$C_j = f(n, V, pitch, D, \dots) \quad (38)$$

Therefore in this section, we first apply Buckingham theorem to determine the problem dimensionless parameters and then achieve a polynomial regression to fit the manufacturer datasheet.

6.1. Application of the Buckingham's theorem

Let us consider the following problem:

$$Thrust = f(\underbrace{D, pitch}_2, \underbrace{\rho_{air}, K, n, V}_4) \quad (39)$$

where K is the air compressibility. Applying Buckingham Theorem leads to following derived expression:

$$C_T = \frac{Thrust}{\rho_{air} \cdot n^2 \cdot D^4} = f'(\beta, J, B) \quad (40)$$

Similar analysis can be conducted replacing *Thrust* by *Power* parameter and following dimensionless set arises:

$$C_P = \frac{Power}{D^5 \cdot n^3 \cdot \rho_{air}} = f'(\beta, J, B) \quad (41)$$

Where for both thrust and power coefficients C_T and C_P :

- $\beta = \frac{pitch}{D}$ is the ratio pitch-diameter.
- $J = \frac{V}{n \cdot D}$ is the advance ratio.
- $B = \frac{K}{\rho_{air} \cdot n^2 \cdot D^2}$ is the air compressibility indicator (similar to Mach number M) and its effect is visible at high speeds.¹

In this section, surrogate models are built to describe the propeller's performance according to (41) in static scenarios ($V = 0$), applicable at the hovering mode and at takeoff, and in dynamic scenarios for the rest of cases where $V \neq 0$.

6.2. Static scenarios, $V = 0$

In the static models, the effect of the advance ratio is removed. In addition, for given aerodynamic configurations, the propeller must adapt its performance by limiting the speed to a certain RPM limit proposed by the manufacturer. For APC MR this operating range remains below 105000 $\frac{RPM}{inch}$.

In Fig. 11, the variation of C_T and C_P for different APC MR Propellers are plotted against β and compressibility factor B . The blue dots correspond to an operation range below the maximum RPM limit (105000 $\frac{RPM}{inch}$), while the black dots show a behaviour beyond that limit.

It can be hypothesized, that there is a relationship between C_T and β (the same with C_P and β), while on the contrary it can be seen how the air compressibility indicator B has a little effect on the propeller performance when the operation range is below the established RPM limit.

Beyond that limit, air compressibility effects begin to have a negative impact on the performance of the propeller with a large increase of the power coefficient (C_P) in comparison with the thrust coefficient (C_T).

The conclusion is that, for a RPM limit lower than 105000 $\frac{RPM}{inch}$, the thrust and power coefficient C_j generally depends on β :

$$C_j \approx f(\beta, B, J) \rightarrow \tilde{C}_j = f(\beta) \quad (42)$$

¹ Considering that $\frac{K}{\rho} = a^2$ where a is the speed of sound, this yields $\frac{a^2}{tip\ speed^2} \propto \frac{1}{M_{tip}^2}$.

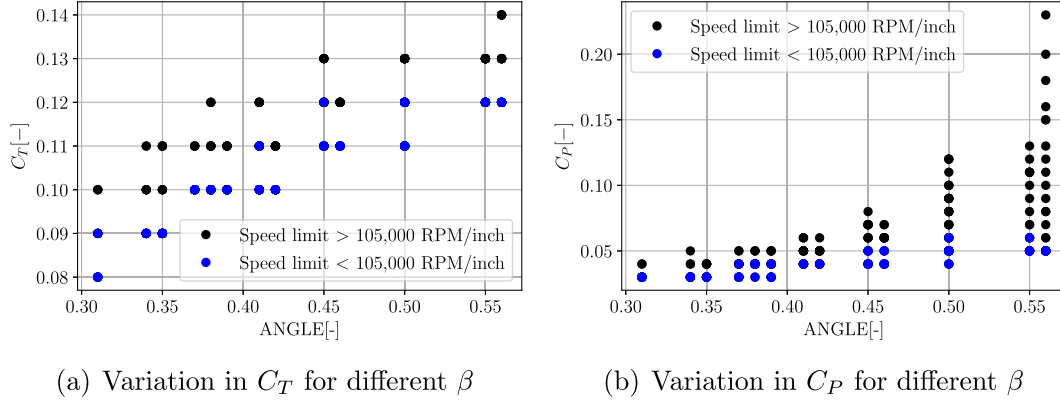


Fig. 11. Evolution of the performance coefficients in static case.

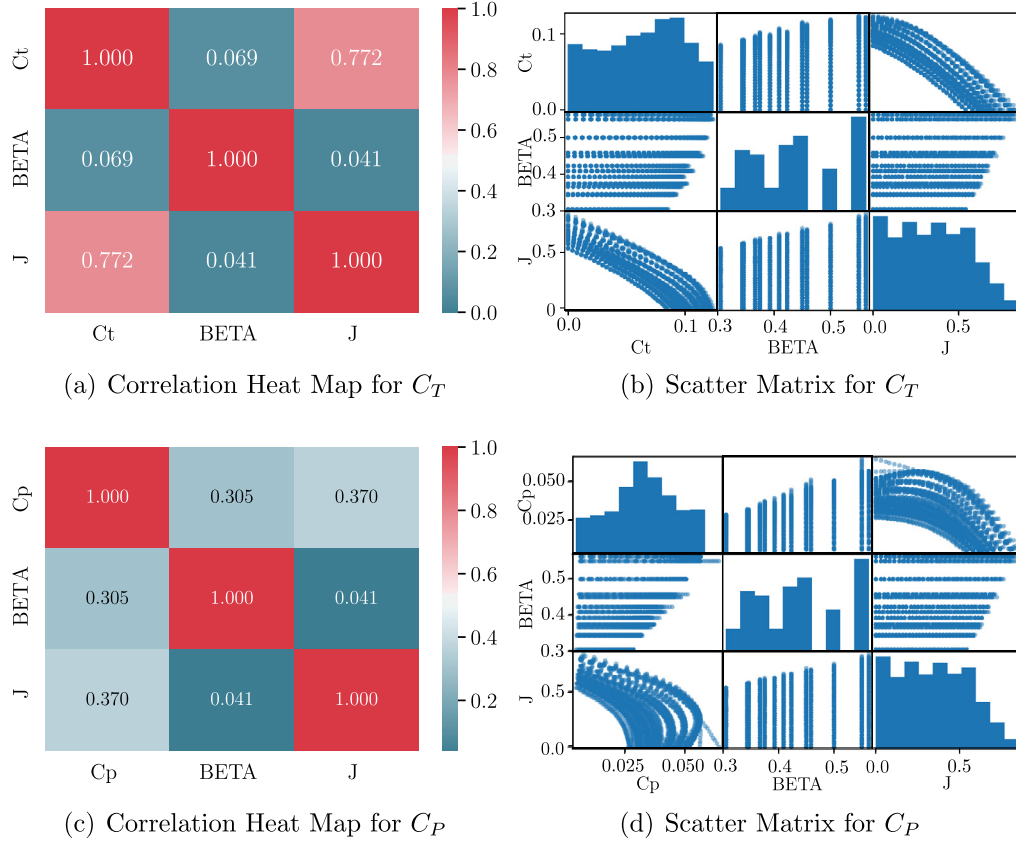


Fig. 12. Multi variable correlation matrix using R^2 heatmap (left) and scatter matrix (right).

The estimated thrust coefficient \tilde{C}_T and power coefficient \tilde{C}_P for an operating range below $105000 \frac{RPM}{inch}$ follow the regression models:

$$\tilde{C}_T = 4.27 \times 10^{-2} + 1.44 \times 10^{-1} \cdot \beta \quad R^2 = 0.946 \quad (43)$$

$$\tilde{C}_P = -1.48 \times 10^{-3} + 9.72 \times 10^{-2} \cdot \beta \quad R^2 = 0.891 \quad (44)$$

with a high value of R^2 , the squared correlation coefficient, fitting the model very well to the data.

For high values of $n \cdot D$, a regression based only on the angle is not very accurate due to the effect of air compressibility. A model for higher RPM should consider the effect of both variables: β and B .

6.3. Dynamic scenarios, $V \neq 0$

According to the Buckingham's theorem, a relationship may be found to link dimensionless parameters:

$$C_j \approx f_j(\beta, J, B) \quad (45)$$

Data are filtered in order to respect manufacturer optimal operating conditions ($n \cdot D \leq 105000 \frac{RPM}{inch}$). Considering such an hypothesis, the compressibility coefficient indicator B effect can be neglected and Equation (45) is approximated by:

$$C_j \approx f_j(\beta, J) = \tilde{C}_j \quad (46)$$

The use of a correlation matrix and the scatter matrix in Fig. 12 help us to visualize that C_T and C_P do not depend on a single parameter:

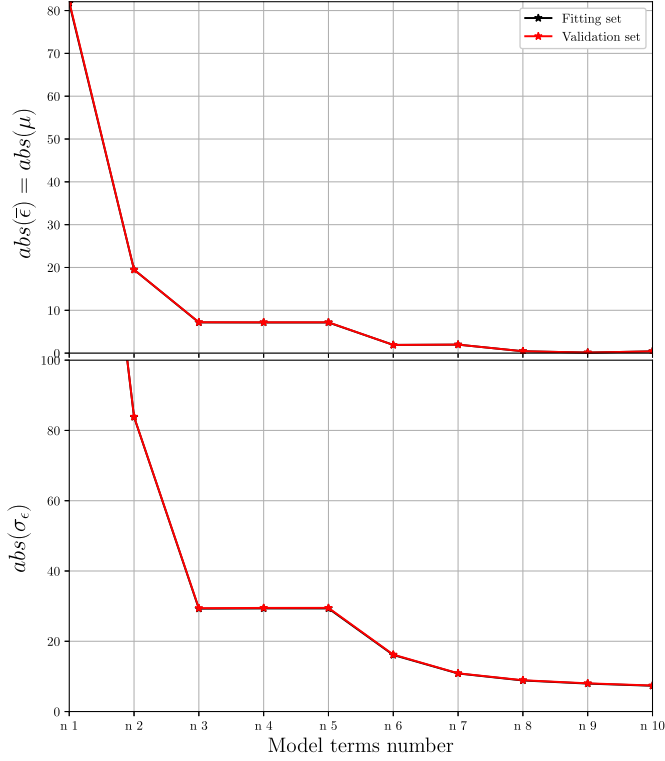


Fig. 13. C_T model relative error $\epsilon = f(\mu, \sigma_\epsilon)$ evolution with terms selection.

Computations have shown that a 3rd order polynomial form can be suitable at early design phases:

$$\begin{aligned} \tilde{C}_{j_{j \in [t, p]}} = & (a_{j,0} + a_{j,1} \cdot \beta + a_{j,2} \cdot J + a_{j,11} \cdot \beta^2 + a_{j,12} \cdot \beta \cdot J \\ & + a_{j,22} \cdot J^2 + a_{j,111} \cdot \beta^3 + a_{j,112} \cdot \beta^2 \cdot J \\ & + a_{j,122} \cdot \beta \cdot J^2 + a_{j,222} \cdot J^3) \end{aligned} \quad (47)$$

When a linear regression is performed on normal-centred values, coefficients absolute value can be used to sort terms by order of importance and regression model can be constructed with increasing complexity (terms number).

As shown in Fig. 13 applied to C_T problem, error may not be reduced after a certain complexity. With APC datasheet, if a 8-terms 3rd order polynomial model is considered, the relative error is limited ($\bar{\epsilon} = 0.4\%$ and $\sigma_\epsilon = 8.8\%$) as shown in Fig. 14:

$$\begin{aligned} \tilde{C}_T = & 0.02791 - 0.06543 \cdot J + 0.11867 \cdot \beta + 0.27334 \cdot \beta^2 \\ & - 0.28852 \cdot \beta^3 + 0.02104 \cdot J^3 - 0.23504 \cdot J^2 \\ & + 0.18677 \cdot \beta \cdot J^2 \end{aligned} \quad (48)$$

Similar results can be obtained considering the C_p parameter ($\bar{\epsilon} = 0.5\%$ and $\sigma_\epsilon = 7.5\%$):

$$\begin{aligned} \tilde{C}_p = & 0.01813 - 0.06218 \cdot \beta + 0.00343 \cdot J + 0.35712 \cdot \beta^2 \\ & - 0.23774 \cdot \beta^3 + 0.07549 \cdot \beta \cdot J - 0.12350 \cdot J^2 \end{aligned} \quad (49)$$

Those \tilde{C}_T , \tilde{C}_p estimators, depicted in Fig. 15, present multiple advantages:

- To be continuous over *pitch* and *D* parameters, which leads to faster optimized design and may converge to specific propeller design.
- To have analytic derivatives.

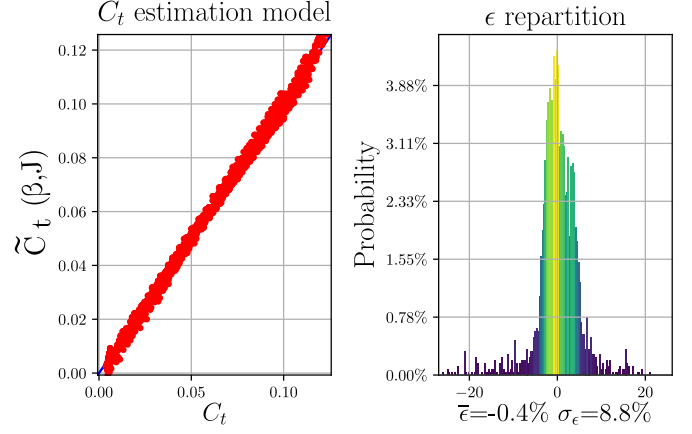
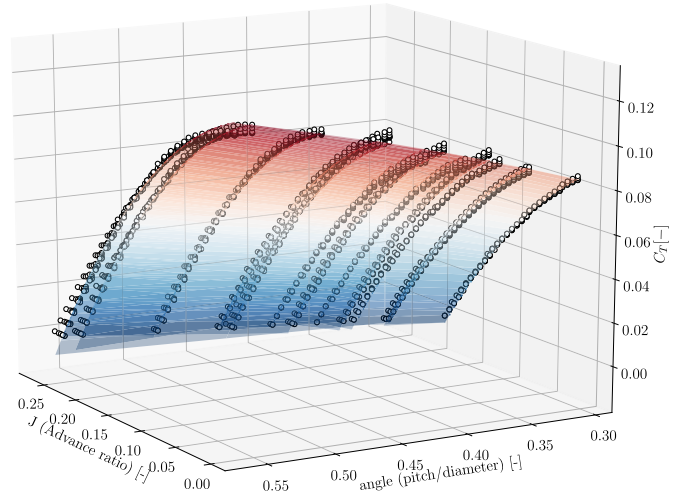
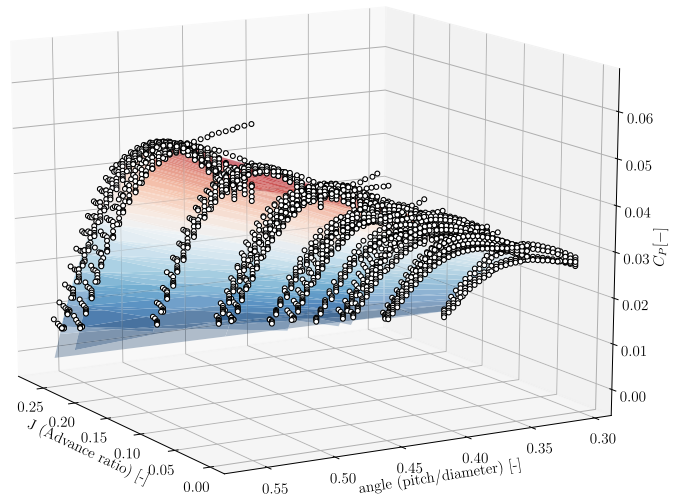


Fig. 14. C_T model performance considering 1st to 8th terms.



(a) 3D plot of Equation 48 and reference dataset



(b) 3D plot of Equation 49 and reference dataset

Fig. 15. 3D regression models of estimated performance coefficients and reference points.

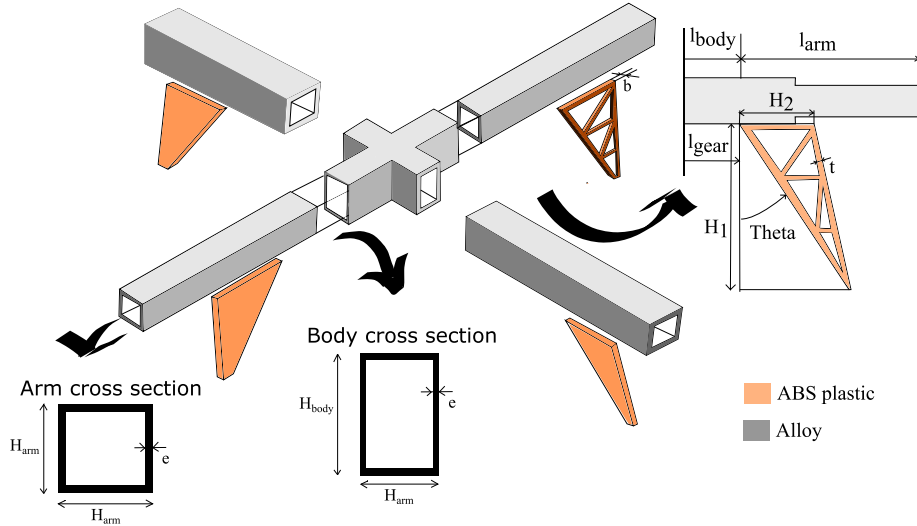


Fig. 16. Simplified structure hypothesis.

- To have regular expressions that can be handled by symbolic parser for different output/inputs alternatives (ex: $pitch = f(C_T, D, n, V)$).

7. VPLM regression applied to structural parts

The UAV structure has a non-negligible impact on its performance since it represents between 25% to 35% of the Maximum Takeoff Weight (MTOW) that includes the payload. Therefore, it is important to have an estimation of the mass of its sub-components: landing gears, frame arms and body.

It is difficult to address the wide range of complex geometries which can be found over the models market. A simple geometry is presented in Fig. 16 for further analysis and calculation steps.

- Body is assumed to be an aluminium or composite cross with hollow rectangle section,
- Arms are made of aluminium hollow bars with square cross section,
- Landing gears are assumed to be printing ABS plastic parts.

The structure is sized with respect to two sizing scenarios: takeoff maximum thrust (arms) and a crash with a given impact speed (body, arms, landing gears).

The first sizing scenario is relatively simple and considering that the body is rigid compared to the arms, the equivalent problem is a l_{arm} length cantilever beam with an applied load $F = Thrust$. The maximum stress is estimated with safety coefficient k_s as:

$$\sigma_{max} = \frac{H_{arm}}{2} \frac{12 \cdot Thrust \cdot l_{arm}}{H_{arm}^4 - (H_{arm} - 2e)^4} \leq \frac{\sigma_{alloy}}{k_s} \quad (50)$$

which can be written with dimensionless arm aspect ratio $\pi_{arm} = \frac{e}{H_{arm}}$:

$$H_{arm} \geq \left(\frac{6 \cdot Thrust \cdot l_{arm} \cdot k_s}{\sigma_{alloy} (1 - (1 - 2 \cdot \pi_{arm})^4)} \right)^{\frac{1}{3}} \quad (51)$$

The second sizing scenario is more complex to consider and is developed in the next subsection.

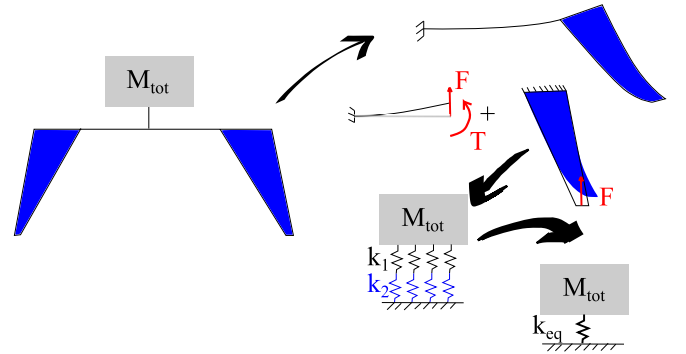


Fig. 17. Equivalent stiffness problem decomposition with 4 landing-gears.

7.1. Crash sizing scenario

The crash sizing scenario considers a maximum speed V_{impact} of the drone when hitting the ground. At such speed the structure should resist (i.e. the maximum stress should not be exceeded) and for higher speeds, the landing gears are the parts that break as structural fuses.

To calculate the equivalent maximum load resisted by the landing gears, the energy conservation law applies the kinetic energy stored in drone mass to potential energy in structural parts transitory deformation:

$$\begin{aligned} \frac{1}{2} k_{eq} \cdot \delta x^2 &= \frac{1}{2} M_{tot} \cdot V_{impact}^2 \\ \Rightarrow F_{max} &= \frac{1}{4} (k_{eq} \cdot \delta x + M_{total} \cdot g) \\ &= \frac{1}{4} (V_{impact} \cdot \sqrt{k_{eq} M_{total}} + M_{total} \cdot g) \end{aligned} \quad (52)$$

To calculate the maximum stress induced by the maximum load F_{max} applied to one landing gear, the equivalent stiffness k_{eq} should be determined. For this purpose, the problem is broken down into simpler structural parts, as depicted in Fig. 17, and the equivalent stiffness k_{eq} is expressed considering the effect of each stiffness on the whole part.

$$k_{eq} = 4 \cdot \frac{\tilde{k}_1 \cdot \tilde{k}_2}{k_1 + k_2} \quad (53)$$

The calculation of the body/arm deformation applies the fixed-beam formulas, while for the landing gear complex geometry a FEM simulations are used to build an analytic model.

7.2. Landing gear stiffness and induced stress estimation applying VPLM

To design landing gear which can be a specific printed ABS part, engineer will face one problem: estimate the applied load in the case of a crash in order to determine the induced stress. But, even before, as the stress depends on the load applied to the landing gear, an estimation of the stiffness \tilde{k}_2 should be established. Therefore, FEM simulations are performed on different geometries ($H_1 \in [5, 20]$ cm, $H_2 \in [1, 10]$ cm, $t \in [3, 15]$ mm, $\theta \in [20, 45]$ deg) with constant thickness b .

If the problem is expressed in regular form:

$$\frac{k_2}{b} = f(\underbrace{H_1, H_2, t}_3, \underbrace{E, \theta}_2) \quad (54)$$

A dimensional analysis leads to the following problem formulation:

$$\pi_{k_2} = \frac{k_2}{b \cdot E} \approx f\left(\pi_1 = \frac{H_1}{H_2}, \pi_2 = \frac{t}{H_1}, \pi_3 = \theta\right) \quad (55)$$

and then:

$$\tilde{k}_2 = \pi_{k_2} \cdot b \cdot E \quad (56)$$

π_{k_2} is fitted by a 2nd order variable power-law expression:

$$\pi_{k_2} = 10^{a_0} \cdot \pi_1^{a_1+a_{11} \cdot \log(\pi_1)+a_{12} \cdot \log(\pi_2)+a_{13} \cdot \log(\theta)} \cdot \pi_2^{a_2+a_{22} \cdot \log(\pi_2)+a_{23} \cdot \log(\theta)} \cdot \theta^{a_3+a_{33} \cdot \log(\theta)} \quad (57)$$

In logarithmic space this formula can be adapted to the following linear form:

$$\begin{aligned} \log(\pi_{k_2}) = & a_0 + a_1 \cdot \log(\pi_1) + a_{11} \cdot \log(\pi_1)^2 \\ & + a_{12} \cdot \log(\pi_1) \cdot \log(\pi_2) + a_{13} \cdot \log(\pi_1) \cdot \log(\theta) \\ & + a_2 \cdot \log(\pi_2) + a_{22} \cdot \log(\pi_2)^2 \\ & + a_{23} \cdot \log(\pi_2) \cdot \log(\theta) + a_3 \cdot \log(\theta) + a_{33} \cdot \log(\theta)^2 \end{aligned} \quad (58)$$

with $x_1 = \log(\pi_1)$, $x_2 = \log(\pi_1)^2 \dots$

After an analysis of the error distribution, it is observed that a 5-terms 2nd order model achieves a sufficient fidelity level (Fig. 18):

$$\pi_{k_2} = 10^{-0.37053} \cdot \pi_1^{-3.11170} \cdot \pi_2^{1.10205} \cdot \theta^{-6.61617-4.86580 \cdot \log(\theta)} \quad (59)$$

A dimensional analysis conducted on constraint σ_{max} leads to following formula:

$$\pi_{\sigma_{max}} = \frac{\sigma_{max} \cdot b \cdot H_1}{F} \approx f\left(\frac{H_1}{H_2}, \frac{t}{H_1}, \theta\right) = f(\pi_1, \pi_2, \theta) \quad (60)$$

Using a 5-terms 2nd order form, the model obtained is:

$$\tilde{\pi}_{\sigma_{max}} = 10^{0.14690} \cdot \pi_1^{2.08982} \cdot \pi_2^{-0.98108} \cdot \theta^{3.38363+2.66468 \cdot \log(\theta)} \quad (61)$$

Therefore, this model enables to predict the mechanical stress generated on the landing gear in the case of a crash. The number of design parameters is reasonable and the prediction is relatively accurate ($\tilde{\epsilon} = 0.1\%$ and $\sigma_{\epsilon} = 4.1\%$) similarly to the rest of the models proposed in this paper.

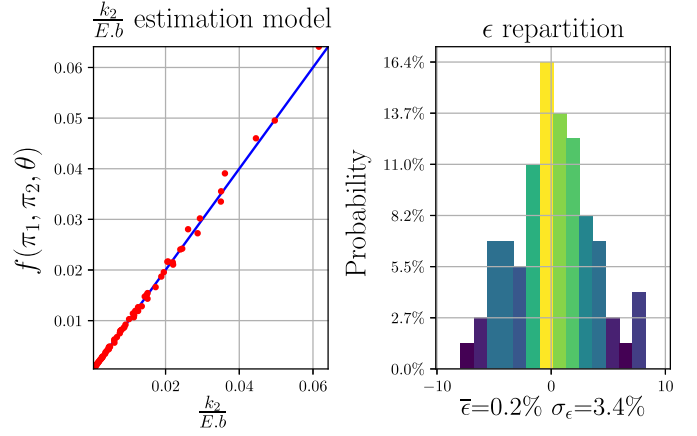


Fig. 18. π_{k_2} model performance considering 1st to 5th terms.

8. Assessment of estimation models performance during preliminary design

The estimation models are the tools that allow us to work in a continuous domain, reducing the work time and eliminating the limitations related to data tables. The use of analytical models also facilitates the implementation of sizing and optimization procedures. Reference [33] explains how to solve the main design problems. Article [34] shows in detail the implementation of a sizing procedure for multicopter drones applying the models described in this article in an optimization routine. The following table gives the specifications and results of the overall drone sizing and the resulting errors when compared to their actual industrial reference. It can be seen that the proposed models allow performing a relevant preliminary design of drones (Table 9).

9. Conclusions


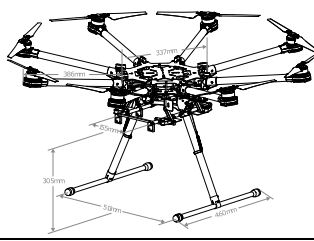
In this paper a set of valid estimation models for the key components of all-electric multicopter drones is presented. One of the main hallmarks of these models lies in its mathematical continuous form, which facilitates the implementation of design and optimization tools. The use of dimensional analysis, apart from providing these physically-motivated approaches with a unified physical basis, gives them greater confidence and understanding compared to other pure statistical approaches in the literature. As a result, scaling laws show robust outcomes in terms of deviation, although it is recommended to follow certain guidelines to reduce such deviation. Based on the current available technologies, they can be applied to the preliminary design of new systems as only a reference value is needed. Surrogate modelling techniques are used in order to obtain an analytic model based on data-sheet data (propellers) and on FEM simulations data (landing gear). In these cases, the dimensional analysis facilitates the choice of the main independent parameters and strengthens the prediction of the models.

The proposition of this new multicopter drone sizing model library is important to perform an overall sizing loop. This is emphasized in the case of high payloads, where the mass of the components increase significantly in order to maintain similar autonomy performance requirements.

Declaration of competing interest

None declared.

Table 9
Drone platforms references and sizing results.

Drone platforms	a) MK-Quadro ^a	b) Spreading Wings ^b
		
Specifications		
Payload:	1 kg	4 kg
Arms/Prop. per arm:	4/1	8/1
Climb speed:	10 m/s	6 m/s
Autonomy:	15 min	18 min
Sizing		
Total mass:	1642 g (+16.5% ref.)	8513 g (-10.3% ref.)
Battery mass:	353 g (+7.29% ref.)	2133 g (+10.4% ref.)
Motor mass:	47 g (-12.9% ref.)	160 g (+1.2% ref.)
Max. Power:	173 W (-1.14% ref.)	449 W (-10.29% ref.)
Diameter propeller:	0.256 m (+2.4% ref.)	0.40 m (+5.26% ref.)

^a MK-Quadro: <http://wiki.mikrokoetter.de/en/MK-Quadro>.

^b Spreading Wings S1000+: <https://www.dji.com/fr/spreading-wings-s1000>.

Acknowledgements

The research was carried out as part of the DroneApp project funded by the RTRA STAE (Sciences et Technologies pour l'Aéronautique et l'Espace, www.fondation-stae.net). The authors gratefully acknowledge the support of François DEFAY.

References

- [1] K.J. Walchko, M.C. Nechyba, E. Schwartz, A. Arroyo, Embedded low cost inertial navigation system, in: Florida Conference on Recent Advances in Robotics, FAU, Dania Beach, FL, May 2003, pp. 8–9.
- [2] M. Logan, J. Chu, M. Motter, D. Carter, M. Ol, C. Zeune, Small uav research and evolution in long endurance electric powered vehicles, in: AIAA Infotech@ Aerospace 2007 Conference and Exhibit, 2007, p. 2730.
- [3] G. Cai, J. Dias, L. Seneviratne, A survey of small-scale unmanned aerial vehicles, in: Recent Advances and Future Development Trends, vol. 2, World Scientific, 2014, pp. 175–199.
- [4] C. Silva, W.R. Johnson, E. Solis, M.D. Patterson, K.R. Antcliff, Vtol urban air mobility concept vehicles for technology development, in: 2018 Aviation Technology, Integration, and Operations Conference, 2018, p. 3847.
- [5] R. Schiavullo, Ehang 184 world first self driving taxi car to flight autonomously at low altitude, *Virtual Real.* 3 (2016) 02.
- [6] Ehang184, autonomous aerial vehicle, <http://www.ehang.com/ehang184/index>. (Accessed 25 March 2019).
- [7] Volocopter reinventing urban mobility, <https://www.volocopter.com/en/>. (Accessed 25 March 2019).
- [8] D. Bershadsky, S. Haviland, E.N. Johnson, Electric multirotor uav propulsion system sizing for performance prediction and design optimization, in: 57th AIAA/ASCE/AHS/ASC Structures, Structural Dynamics, and Materials Conference, 2016, p. 581.
- [9] O. Gur, A. Rosen, Optimizing electric propulsion systems for unmanned aerial vehicles, *J. Aircr.* 46 (4) (2009) 1340–1353.
- [10] Mk-quadro – mikrokoetterwiki, <http://wiki.mikrokoetter.de/MK-Quadro/>. (Accessed 25 March 2019).
- [11] The mk8-3500 standard, <http://www.mikrokoetter.de/en/products/nmk8stden/nmk8ueb%eren>. (Accessed 25 March 2019).
- [12] DJI – the world leader in camera drones/quadcopters for aerial photography, <https://www.dji.com/en/spreading-wings-s1000/spec>. (Accessed 25 March 2019).
- [13] N.A. Vu, D.K. Dang, T. Le Dinh, Electric propulsion system sizing methodology for an agriculture multicopter, *Aerosp. Sci. Technol.* 90 (2019) 314–326.
- [14] D. Shi, X. Dai, X. Zhang, Q. Quan, A practical performance evaluation method for electric multicopters, *IEEE/ASME Trans. Mechatron.* 22 (3) (2017) 1337–1348.
- [15] B.-S. Jun, J. Park, J.-H. Choi, K.-D. Lee, C.-Y. Won, Temperature estimation of stator winding in permanent magnet synchronous motors using d-axis current injection, *Energies* 11 (8) (2018) 2033.
- [16] C. Ampatis, E. Papadopoulos, Parametric design and optimization of multi-rotor aerial vehicles, in: Applications of Mathematics and Informatics in Science and Engineering, Springer, 2014, pp. 1–25.
- [17] P. Wei, Z. Yang, Q. Wang, The design of quadcopter frame based on finite element analysis, in: 3rd International Conference on Mechatronics, Robotics and Automation, Atlantis Press, 2015, pp. 1353–1356.
- [18] S.K. Phang, K. Li, K.H. Yu, B.M. Chen, T.H. Lee, Systematic design and implementation of a micro unmanned quadrotor system, *Unmann. Syst.* 2 (02) (2014) 121–141.
- [19] S. Bouabdallah, Design and control of quadrotors with application to autonomous flying, Tech. rep., EPFL, 2007.
- [20] eCalc, eCalc, the most reliable rc calculator on the web, <https://www.ecalc.ch/>. (Accessed 25 March 2019).
- [21] M. Holmes, Introduction to the Foundations of Applied Mathematics, 2009, pp. 1–42.
- [22] E. Groesen, J. Molenaar, Continuum Modeling in the Physical Sciences, vol. 13, 2007, pp. 1–29.
- [23] M. Jufer, Design and losses, in: Scaling Law Approach, The Nordic research Symposium on Energy Efficient Electric Motors and Drives, 1996, pp. 21–25.
- [24] M. Budinger, J. Liscouët, F. Hospital, J. Maré, Estimation models for the preliminary design of electromechanical actuators, *Proc. Inst. Mech. Eng., G J. Aerosp. Eng.* 226 (3) (2012) 243–259.
- [25] C.P. Steinmetz, On the law of hysteresis, *Proc. IEEE* 72 (2) (1984) 197–221.
- [26] G. Lakkas, Mosfet power losses and how they affect power-supply efficiency, *Analog. Appl.* 10 (2016) 22–26.
- [27] X. Giraud, M. Budinger, X. Roboam, H. Piquet, M. Sartor, J. Faucher, Optimal design of the integrated modular power electronics cabinet, *Aerosp. Sci. Technol.* 48 (2016) 37–52.
- [28] F. Sanchez, S. Delbecq, M. Budinger, I. Hazyuk, Modelling and design approaches for the preliminary design of power electronic converters, in: *Electronics 2017*, Toulouse, France, 2017.
- [29] S. Lemon, A. Miller, Electric Vehicles in New Zealand: Technologically challenged, University of Canterbury New, Electric Power Engineering Centre (EPE-Centre), 2013.
- [30] D. Lacey, C. Steele, The use of dimensional analysis to augment design of experiments for optimization and robustification, *J. Eng. Des.* 17 (1) (2006) 55–73.
- [31] F. Sanchez, M. Budinger, I. Hazyuk, Dimensional analysis and surrogate models for the thermal modeling of multiphysics systems, *Appl. Therm. Eng.* 110 (2017) 758–771.
- [32] E. Motors, Performance data | apc propellers, <https://www.apcprop.com/technical-information/performance-data/>. (Accessed 25 March 2019).
- [33] A. Reyssat, M. Budinger, J.-C. Maré, Computer-aided definition of sizing procedures and optimization problems of mechatronic systems, *Concurr. Eng.* 23 (4) (2015) 320–332.
- [34] S. Delbecq, M. Budinger, A. Reyssat, A. Ochotorena, Efficient sizing and optimization of multirotor drones based on scaling laws and similarity models, *Aerosp. Sci. Technol.*, submitted for publication.